

Volume quantification in interphase voxels of ore minerals using 3D imaging

Da Assuncao Godinho, J. R.; Kern, M.; Renno, A.; Gutzmer, J.;

Originally published:

December 2019

Minerals Engineering 14(2019), 106016

DOI: <https://doi.org/10.1016/j.mineng.2019.106016>

Perma-Link to Publication Repository of HZDR:

<https://www.hzdr.de/publications/Publ-30075>

Release of the secondary publication
on the basis of the German Copyright Law § 38 Section 4.

CC BY-NC-ND

Volume quantification in interphase voxels of ore minerals using 3D imaging

J. R. A. Godinho,^{*a} M. Kern^a, A. D. Renno^a, J. Gutzmer^a

* corresponding author, j.godinho@hzdr.de

^a Helmholtz-Zentrum Dresden-Rossendorf, Helmholtz Institute Freiberg for Resource Technology, Chemnitz Straße 40, 09599 Freiberg, Germany

Abstract

This contribution presents and validates a new method to correct for the main limitations of volume quantification using X-ray computed tomography: limited spatial resolution and lack of mineralogical classification. The volume of a phase of interest (cassiterite, SnO₂) is calculated using the intensity of voxels at interphases, which are typically the regions of main uncertainty in 3D imaging. Instead of traditional segmentation methods that define boundaries between phases, our method considers interphases as regions that can be several voxels across. The method is validated using a feedback loop between 2D scanning electron microscopy-based image analysis and bulk chemical analysis where the advantages of each technique are used to correct for the limitations of another. The percent of cassiterite derived from our method are within 10 % deviation from those measured by scanning electron microscopy-based image analysis and bulk chemical analysis, when the P₅₀ of the particle size distribution is at least 5 times the voxel size of the scan, which is a better agreement than results derived from other segmentation methods. Therefore, our method reduces the uncertainty of volume quantification and lowers the limit of grain sizes for which volumes can be reliably measured using computed tomography. The reduced uncertainty and bias can contribute to broadening the application of 3D imaging to mineral engineering as complementary to well established techniques.

Keywords: partial volume effect, computed tomography, mineral processing, raw materials, X-ray imaging, geometallurgy.

1. Introduction

X-ray computed tomography (CT) is the prime technique for non-invasive 3D imaging used in research and industry (Ketcham and Carlson, 2001; Maire and Withers, 2014). For example, in medicine to track tumour growth (Haines et al., 2009), in materials science to investigate materials failure (Wang et al., 2017a), and in oil and gas exploration to analyse pore scale processes in rocks (Lin et al., 2016). In mineral process engineering, CT was shown to provide unique insights about the grain size, surface area, spatial distribution and association of minerals (Miller et al., 2009; Wang et al., 2017b; Reyes et al., 2018; Miller and Lin, 2018). For example, the grain sizes and the liberated surface area covering the entire grain can be derived from 3D images, while traditional 2D scanning electron microscopy-based image analysis (aka automated mineralogy), only gives information about a small fraction of the grains leading to an underestimation of grain sizes (Reyes et al., 2017) and a potentially overestimated liberation analysis (Wang et al., 2018). Additionally, since CT does not require sample preparation, the distribution of grains in a rock is preserved so that spatial correlations can be studied, which is not possible using destructive bulk analytical methods. Despite the additional information in 3D images, CT is not commonly used to quantify the volume fraction of minerals in mineral process engineering. This is possibly due to limitations inherent to small grain sizes of ore minerals e.g., particles are typically beneficiated at sizes between 5 and 300 µm (Wills and Finch, 2016), which leads to a high uncertainty of volume quantification. Additionally, the polyphase composition of ores, typically containing more than 10 discrete minerals, does not allow direct identification of minerals based on the relative grey-scale of CT datasets.

In industrial mineral beneficiation the volume of ore particles correlates directly to profit, thus the uncertainty of measuring volume fractions using CT is unacceptable for decision making. Instead, bulk chemical analyses, often in combination with X-ray powder diffraction (Parian et al., 2015; Silva et al., 2018), are used to quantify the concentration of chemical elements and minerals present in a sample, but no information about the spatial distribution of minerals (i.e. mineral association and liberation) can be derived from these methods. Automated mineralogy is used to map the composition of surfaces, which reveals the modal mineralogy with high spatial resolution (Fandrich et al., 2007). However, the spatial information from surfaces may not be fully representative of the 3D rock volume (Cordes et al., 2015; Ueda, 2018) and the required sample preparation may add bias to results. Data from bulk chemical analysis and automated mineralogy can be compared and reconciled for a more comprehensive description of the chemical and mineralogical composition (Chryssoulis and Cabri, 1990; Kern et al., 2018a; Frenzel et al., 2019). Nevertheless, it is difficult to assess if 2D imaging and bulk chemical analysis yield better results than CT if the different techniques are not validated against each other. Without comparing the results it is difficult to infer that either 3D data is necessarily more representative than 2D, or that the higher resolution of 2D imaging will necessarily yield more accurate quantification than lower resolution CT (Reyes et al., 2017). In conclusion, broadening the application of CT to mineral process engineering – in particular to mineralogical complex, fine-grained ores - demands validation using well established 2D-imaging and bulk chemical techniques, as well as the demonstration of the advantages of CT as complementary to those techniques.

In this paper, we propose a new method to reduce the bias and the error associated to the volume quantification of small grains using CT (**Section 3**). The method is demonstrated using a tin ore where the mineral of interest is cassiterite, SnO_2 . The first step is to classify the minerals in the sample based on the voxels' intensity by correlation with SEM-based image analysis (**Section 4.1**). A sequence of steps is proposed to segment voxels at the interphases of cassiterite grains and to label those voxels based on their neighbouring phase (**Section 4.2.1**). The volume fraction of cassiterite in a voxel is derived from its intensity using an equation that depends on the neighbour phase (**Section 4.2.2**). Results from our method are compared to those derived from automatic segmentation methods (**Section 4.2.2**), and are validated by correlation with SEM-based analysis as well as chemical assays (**Sections 4.2.3**). Finally, the method is used to quantify the volume of cassiterite in an uncrushed specimen (**Section 4.3**). We expect the reduced bias and uncertainty of measuring the volume of small grains of dense minerals, typical of ores, will broaden the application of 3D imaging to mineral beneficiation and geometallurgical research in the raw materials community (**Section 5**).

2. Materials and Methods

Samples originate from the skarn orebody of the Hämmerlein deposit (Erzgebirge, Germany). Cassiterite is accompanied by a characteristic chlorite-fluorite-sulphide assemblage that overprints and sometimes replaces silicate- and/or iron oxide-dominated lithounits (Kern et al., 2018b). A bulk sample of several tons from the +590 m level of the mine was crushed and ground to 100 % < 630 μm . Subsequently it was classified into three particle size fractions (0-100 μm , 100-250 μm , 250-630 μm). One 30 mm diameter grain mount was prepared for each size fraction (GM<100, GM250 and GM630), by mixing 1 g aliquots with the same volume of graphite and epoxy resin. While the epoxy cures, gravity settling is expected due to the discrepancy in densities between cassiterite ($\rho > 6.9 \text{ g/cm}^3$) and silicates minerals, such as quartz ($\rho = 2.65 \text{ g/cm}^3$). To prevent bias caused by such settling, the grain mounts were cut into vertical slices, which were turned 90 degrees, re-embedded and polished (Heinig et al., 2015). In this manner, the so-called B-sections are used for surface analysis. Cassiterite in the Hämmerlein ore is fine-grained and brittle, thus its concentrations in the fine fraction are higher than in the coarse fraction. The particle size distribution of the three granular samples was measured using a laser diffractometer

(Sympatec, Clausthal-Zellerfeld, Germany, **Figure A.1**). In addition to the bulk sample, a hand specimen from the same location was cut to a block of approximately 4.2 × 2.4 × 0.5 cm size.

The three polished grain mounts were analysed with scanning electron microscopy (SEM)-based image analysis using a Mineral Liberation Analyzer (MLA, FEI Company, Hillsboro, OR, USA) (Gu, 2003). The instrument is a FEI Quanta 650F field emission SEM (FE-SEM) equipped with two Bruker Quantax X-Flash 5030 energy dispersive X-ray detectors. Quantitative mineralogical and textural data is extracted from particle maps, which are used to derive the modal mineralogy, bulk geochemistry and mineral associations (Hoal et al., 2009). The grain-based X-ray mapping (GXMAP) mode was used with a resolution of 6 µm/pixel (Fandrich et al., 2007). Back-Scattered Electron (BSE) images were collected with a resolution of 1 µm/pixel. Data was processed with the software package MLA Suite 3.1.4.686 applying the modified approach for automated mineralogy described by Kern et al. (2018).

Bulk geochemical analysis of 10 g aliquots of the particle size fractions were supplied by ALS Limited (Ireland). The samples were pulverized to 85 % passing 75 µm. Eight major and minor oxides (SiO₂, Al₂O₃, Fe₂O₃, CaO, MgO, Na₂O, K₂O, TiO₂) were analysed by inductively coupled plasma optical emission spectroscopy (ICP-OES) following a lithium borate fusion and dilute acid digestion of 2 g sample pulp. Total S contents were determined using a Leco combustion furnace. Sn contents were determined by X-ray fluorescence spectrometry using 5 g sample powder aliquots prepared with glass beads, lithium tetraborate and lithium metaborate as fusion flux. For quality control purposes, reference samples of known composition were analysed for Sn with the same method. Deviations from reference values remained below 10 % (relative) in all cases (Kern et al., 2018a).

Samples were scanned in a CoreTom CT scanner from XRE (Tescan) at 170 keV using two filters mounted at the source, one 0.5 mm copper and one 0.2 mm steel. Samples GM630 and GM250 were scanned at three different voxel sizes: 9.1, 18.2 and 27.3 µm. Sample GM<100 was only scanned with a voxel size of 9.1 and 18.2 µm. Therefore, a total of eight datasets were available for this study, each with a specific particle to voxel size ratio. In addition, the block was scanned with a voxel size of 12.1 µm, limited by the block diameter. Throughout the article, the rounded voxel size will be tagged to the sample name, e.g. GM630_9. The beam current used for scans with each voxel size was optimized so that the resolution is limited by geometrical factors and not by the spot size of the beam.

Reconstructions were done using the Octopus commercial software package. The same reconstruction parameters were used for all scans, which assures the histograms of all reconstructed datasets are comparable. A small beam hardening correction of 0.1 was used to homogenize the grey-scale values throughout the sample, and a scattering correction of 0.08 was used to reduce artefacts. The range of intensity values of raw projections was clipped between 0 and 19 (a relative scale internal of Octopus). This assures each phase appears within the same intensity range in all datasets.

3. Method description

3.1. Defining uncertainty and bias in CT

3D images generated by CT consist of voxels, each with an intensity value, typically shown as grey-scale where brighter means the voxel is part of denser phases and darker means part of lighter phases. In an ideal case, the intensity of each voxel is a function of the X-ray attenuation of the material inside the voxel. At the boundary between two phases, voxels usually contain both phases so that the intensity of the voxel is proportional to their volume fraction. This is the so-called partial volume effect (Goodenough et al., 1986; Ketcham and Carlson, 2001). However, in practice, the intensity of a voxel may also be affected by scanning variability (Lin et al., 2015), e.g.

oscillation of the X-ray source; by stochastic processes, e.g. scattering; and by reconstruction and cone beam artefacts (Ketcham and Carlson, 2001; Boas and Fleischmann, 2012). An important artefact is caused by the penumbra effect that is caused by the fact that the X-ray source is not a point but a spot with some diameter (Kueh et al., 2016). This means that the projection of a point in the sample may be measured across several pixels on the detector. The penumbra effect enhances the partial volume effect causing the typical sense of blurred interphases across 3-5 voxels (for optimal experimental conditions), which in practice means the boundary between two phases is not defined by a single voxel boundary but by several voxels across as a gradient of intensities.

The difficulty to define the exact boundary between phases based on the intensity of voxels is exemplified in a cross section of a 3D volume containing three phases with distinguishable X-ray attenuation contrast (**Figure 1**). Voxels representing a mineral can be labelled from the range of intensity values found at the centre of a grain that are unaffected by the interphase, defined here as bulk voxels, e.g. red, purple or blue phase. Between grains (at interphases), the intensity of voxels ranges between the intensity of bulk voxels characteristic of the neighbour phases. These voxels are defined here as interphase voxels (pink in **Figure 1**). The volume of interphase voxels enclosing a phase define the uncertainty of the volume measurement (Godinho and Withers, 2018). In the given example, the uncertainty of volume associated to the red phase could be larger than the actual measured volume because the size of the grain is close to the voxel size of the scan.

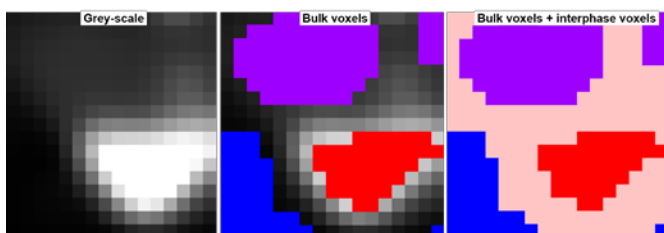


Figure 1: 2D cross section of an arbitrary 3D image showing three phases (blue, purple and red) with different attenuation contrast (different grey values). Note the gradual variation of intensity between bulk voxels across several interphase voxels (pale red). Spatial and intensity scales are redundant in this example.

To discuss the relation between uncertainty and particle size we define *ParVox* as the particle size to voxel size ratio of each dataset (**Eq. 1**). The P_{50} size (50 vol. % of particles are passing this sieve size) is used as reference. We realise that relating resolution with grain sizes would be preferable to particle sizes since some cassiterite grains are embedded into larger particles (**Figure 2**). However, MLA underestimates grain sizes due to stereological problems, and CT overestimates grain diameters due to particle agglomeration at the bottom of the grain mount and by definition, interphase voxels extend the real boundary of grains. Therefore, no reliable measurement of grain sizes could be obtained. In this case, *ParVox* gives an indication of the voxel size necessary to have a reasonable volume quantification of grains with a given size. The overestimation of this grain size should be lower for smaller particle size fractions.

$$ParVox = \frac{Particle\ size}{Voxel\ size} \quad \text{Eq. 1}$$

The decision about whether an interphase voxel belongs, for example, to the red or to the blue phase, would typically be done by defining a threshold above which the voxel belongs to the red phase and below which the voxel belongs to the blue phase. The choice of threshold values is a major source of segmentation bias. If a partially filled voxel at the red-blue interphase is labelled as red, the full voxel volume is accounted for the total volume of red; and contrarily, if labelled as blue, it is not accounted for the total volume of red. Consequently, the total volume of the red phase can be over- or underestimated, and it is difficult to estimate the resulting error. To reduce the bias,

specific criteria can be used to automatically define the thresholds of a phase (Sezgin and Sankur, 2004). Threshold values can be derived from the peaks of the histogram (Glasbey, 1993) or from the distribution of intensity scale, e.g. entropy methods. To refine the segmentation of a phase, besides the intensity values, additional local information from neighbour voxels can be used to define phase boundaries (Goodenough et al., 1986; Glover and Pelc, 1980; Wang et al., 2017b; Heckel et al., 2014; Soullaine et al., 2016). For example, by computing the grey-scale gradients, an image can be subdivided in regions with common grey-scale properties. Within each region, the boundary of a phase can be found from abrupt changes of intensity, e.g. hysteresis method (Jayasree et al., 2018), or using morphological operations, e.g. watershed methods (Kornilov and Safonov, 2018). In practice, the hysteresis and watershed methods allow for a more flexible choice of interphase voxels, for example, a voxel with an intensity below the threshold that defines the phase can be segmented as part of the phase if it is within the region defined by, for example, a gradient operation. Although automatic segmentation methods reduce bias, depending on the method and criteria used, results may vary significantly. In conclusion, the result from the same CT dataset is strongly dependent on how the boundaries between phases are processed.

3.2. New method

We propose an alternative empirical method to quantify the volume of mineral phases. Instead of defining sharp boundaries between phases, our method considers the interphase as a region, some voxels across. The method is based on the hypothesis that the intensity of interphase voxels is linearly proportional to the volume fraction of the phases on each side of the interphase. For example, at the red – blue interphase, the intensity of interphase voxels is higher than the intensity of the bulk blue phase; whereby the difference between the intensity of interphase and bulk voxels is proportional to the volume of red phase. In practice, there is a discrepancy between the real space and its virtual representation by CT data that is caused by the artefacts described above. Therefore, the hypothesis supporting this method implies that those artefacts are anti-symmetric. That is, on one side of the interphase the volume of a dense phase is virtually exaggerated (manifested by a higher voxel intensity) by the same amount than the volume of the same phase is virtually lower on the other side of the interphase (manifested by a lower voxel intensity).

Our method assumes that two points are generally known in the relation between volume fraction vs intensity: the intensity of, for example, bulk red voxels correspond to volume fraction 1 (100% red, 0% blue), and the intensity of bulk blue voxels correspond to volume fraction 0 (0% red, 100% blue). It is also assumed that the values between volume fraction 0 and 1 are given by the linear regression between those two points (intensity vs volume fraction). This linear correlation depends on the intensity of bulk voxels of each phase neighbouring the phase of interest. For example, the intensity of voxels at the red – blue and the red – purple interphases follow a different gradual evolution (**Figure 1**). In practice, this means that a voxel in the red – blue interphase contains more red than a voxel with the same intensity in the red – purple interphase because the blue phase is defined by intensities lower than the purple phase. This is an improvement to traditional segmentation methods that assume that voxels with the same intensity have the same volume fraction of a phase, either 0 or 100%. In conclusion, to implement our method it is necessary to identify the phases neighbouring cassiterite grains.

4. Results

4.1. Mineral classification of CT data

Here, the CT intensity scale is correlated to MLA and BSE images to classify voxel intensity ranges into mineral groups. The mineral assemblage as measured by MLA (**Table A.1**) can be logically simplified into three groups (**Figure 2**): *Lighter Minerals* (2.6 – 3.7 g/cm³) consisting of quartz, feldspar, amphibole, mica, chlorite, garnet, epidote, fluorite and carbonates (blue); *Denser Minerals* (4.0 – 6.0 g/cm³) consisting of hematite, magnetite, sphalerite, arsenopyrite, chalcopyrite and pyrite

(purple); *Cassiterite* ($>6 \text{ g/cm}^3$, red). Other phases denser than 6 g/cm^3 such as galena account for < 0.002 volume percent of the total mass and exist as grains smaller than $5 \mu\text{m}$.

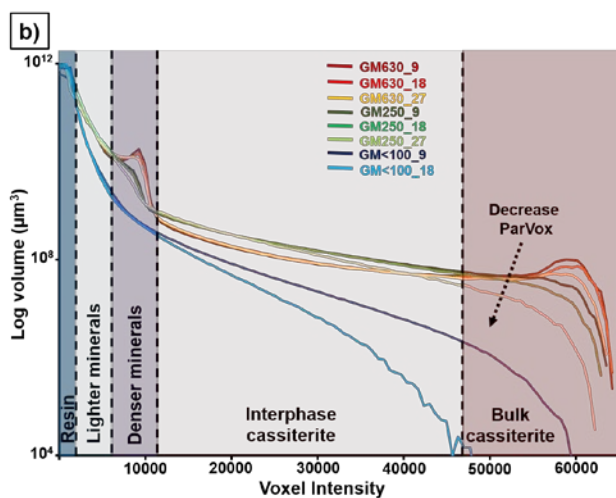
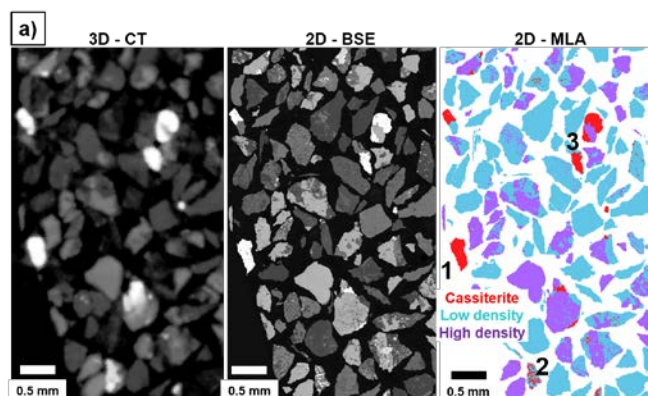


Figure 2: Classification of the CT intensity scale. **a)** Correlation of BSE and MLA images with a CT cross-section about $30 \mu\text{m}$ under the surface of the grain mount. The grey-scale of the cross section is clipped at 20000. Epoxy resin is shown as white space between particles in the MLA image and as black in BSE and CT images. **b)** Histograms from 3D images. Lines of the same colour correspond to the same sample, and lighter tones of the same colour correspond to lower voxel sizes (9.1 , 18.2 and $27.3 \mu\text{m}$). Background coloured regions mark the intensity ranges of the different mineral groups. Note that the total volume of particles in each grain mount is different, so the absolute areas under the curve are only directly comparable for the same sample.

The interval of intensities that represent each mineral group in CT data can be defined by comparing the surface analysed by MLA and BSE to the corresponding cross-section of the 3D image (**Figure 2**). This is a reasonable approach (Burnett et al., 2014; Reyes et al., 2017; Furat et al., 2018), since both scales are a function of the electron density in the sample. Nevertheless, the lower resolution, higher noise and artefacts typical of CT images cause the broadening of the interval of intensities that represent each mineral, which may challenge the correlation of grey-scales. For example, grains may be resolved by BSE with $1 \mu\text{m}$ pixel size, but not by CT with voxel size $>9.1 \mu\text{m}$ (e.g. particle 2, **Figure 2a**). To minimize these limitations, the mineralogical classification of intensity intervals should be done using the larger particles available and the best resolution possible. To avoid artefacts typically found at surfaces analysed by CT, the cross-section of the CT dataset chosen for comparison differs from the surface analysed with MLA by 3 - 4 voxels ($\sim 30 \mu\text{m}$ into the sample). This is acceptable since the particles are 250 - $630 \mu\text{m}$, thus most particles are easily correlated, although, smaller features may not exactly match.

The histogram of sample GM630 shows two peaks at intensities around 9500 and 60500 , and a band at lower intensities (**Figure 2b**). Voxels with intensities above 11500 are found only in areas identified as cassiterite by MLA. Voxels with intensities above 46000 , are found only within larger

cassiterite grains, i.e. bulk voxels that are disconnected from the neighbour phases by at least three voxels thick interphase. Voxels with intensities between 11500 and 46000 are present mostly at the interphases of cassiterite grains and often represent small grains (note the difference in grey-level between particle 1 and 2, **Figure 2a**). Voxels representing denser minerals have intensities always below 11500, and englobe the peak intensities around 9500. The band at lower intensities encompasses the epoxy and the lighter minerals. Although a significant overlap exists, most resin is represented by voxels with intensities below 2100, and few voxels representing lighter minerals have intensities below 2100. No voxels representing lighter minerals have intensities above 6000. It is concluded that five phases can be classified (five coloured regions in the background of the histogram, **Figure 2b**): bulk cassiterite, >46000 (red); interphase cassiterite, 11500-46000 (pale red); denser minerals, 6000-11500 (purple); lighter minerals, 2100-6000 (light blue); and resin, <2100 (dark blue).

The arrow in **Figure 2b** highlights the decrease of the peak, only prominent for sample GM630, corresponding to bulk cassiterite for lower *ParVox*. The lesser volume of bulk cassiterite (red region) is accompanied by an increased volume of interphase cassiterite (pale red region), e.g. compare red lines. Hence, part of the cassiterite detected as bulk voxels at higher resolutions is detected as interphase voxels at lower resolutions. This anticipates the difficulty of traditional segmentation methods to provide a consistent quantification of cassiterite for samples with different *ParVox*. Sample GM<100 has fewer bulk cassiterite voxels for both resolutions analysed.

4.2. New method

4.2.1. Segmentation of interphase voxels

In this section, a workflow of 3D image processing functions is suggested with the goals of labelling bulk cassiterite voxels and interphase cassiterite voxels depending on the neighbour phase. The specific workflow used to label the cassiterite voxels is not universal for the new method and should be adjusted to the characteristics of a sample, e.g. particle size and shape. In our samples cassiterite is present in different sizes, therefore, a flexible workflow was chosen. The individual steps and image processing functions are explained in detail in the Appendix (**Figures A.2-A.4**).

A non-local-means filter (search window = 21, neighbourhood = 3 and difference = 0.4) was applied to the raw data and five phases (bulk cassiterite, interphase cassiterite, denser minerals, lighter minerals and resin) were labelled by “threshold” using as input the intensity ranges found in **Section 4.1**. Additional processing (Appendix) was necessary to segment voxels associated to the interphase of cassiterite grains that have intensities between 6000 and 11500 (denser minerals) and between 2100 and 6000 (lighter minerals). Then, phases labelled as lighter mineral, denser mineral or resin were dilated, resulting in an overlap between interphase cassiterite voxels and their neighbour phase. In case of overlap with more than one neighbour phase, a single label per voxel is determined by the neighbour with the highest intensity. For example, if a voxel is labelled both as neighbouring a dense mineral and resin, the label is set to neighbouring a dense mineral. Note that this is a simplification of the sample where voxels may contain more than two phases.

Resolution and particle size have a notorious impact on the segmentation result (**Figure 3, bottom row**). Cassiterite in GM630 is mostly labelled as bulk cassiterite since most grains are much larger than the voxel size. Most small grains are detected and labelled as interphase cassiterite. Some small grains that are detected at higher resolution are missing at lower resolution (e.g. white arrow), an effect that is observed for the three samples. This is a consequence of the workflow that only allows identifying grains if at least one voxel has intensity above 11500. In sample GM250, particles are more densely packed than in sample GM630. Due to the small size of particles in sample GM<100, the resin and low density minerals are indistinguishable and some denser minerals may be misclassified as lighter minerals. This results in an over-segmentation of the light minerals (most interphase voxels labelled as light blue). Note that sample GM<100 has a particle

size distribution where 24 % of particles are below 9 μm and 50 % are below 27 μm in diameter (**Figure A.1**).

It is not surprising that the same sample at different resolutions has a different label for a voxel in a similar region. That is because larger voxels are more likely to contain mixed phases, thus the voxel intensity may be shifted from the intensity range of pure phases. For example, if two cassiterite grains are separated by a layer of resin with thickness close to the voxel size, an interphase voxel may be labelled as neighbouring resin at high resolution and labelled as neighbouring denser minerals at lower resolution, e.g. red arrows in **Figure 3**. Contrarily, traditional segmentation methods that define a boundary between phases would attribute volume fractions of 0 or 1 to any voxel, even at the uncertain interphase.

The edges of cassiterite grains are seemingly over-segmented (**Figure 3**) since all interphase voxels are accounted. This is more noticeable for smaller grains and for lower resolutions where interphases are less sharp. For example, the space between near cassiterite grains cannot be resolved at lower resolutions as pointed by red arrows. Voxels in the unresolved area have a grey-scale between that of cassiterite (white) and dense minerals (light grey), and hence, contain only some volume fraction of cassiterite that is accounted as an interphase voxels. This way, the partial volume of voxels with only a small fraction of cassiterite remains accounted for at lower resolution and the over-segmentation of cassiterite grains does not translate into an overestimation of cassiterite volume, as will be shown in **Section 4.2.3**.

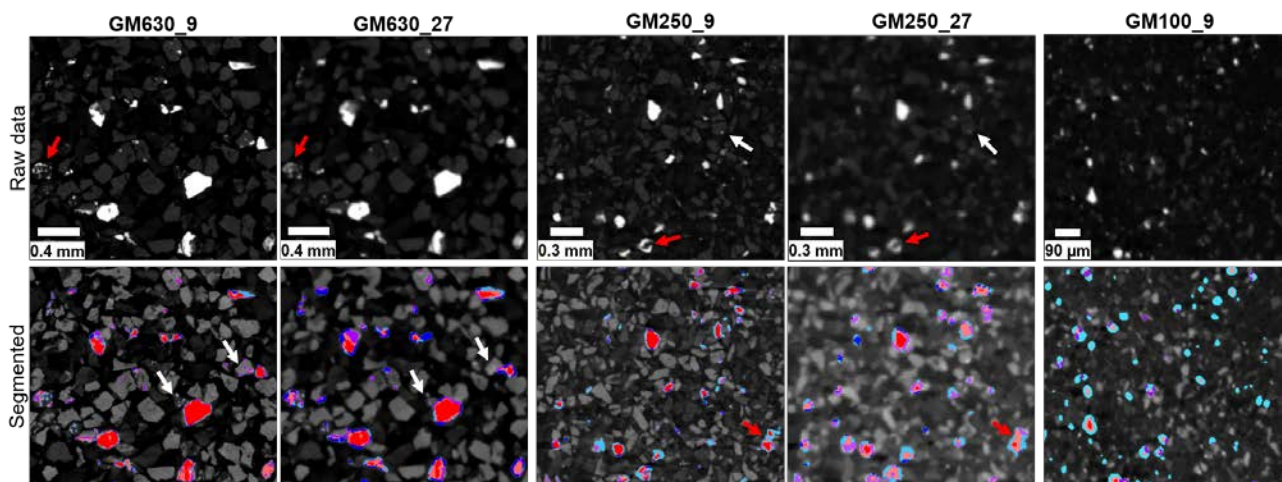


Figure 3: Cross-sections from CT datasets before (top row) and after segmentation (bottom row). Colours identify different phases: resin, dark blue; light minerals, light blue; dense minerals, purple; and cassiterite, red. The grey scale of top row is clipped at 46000 to highlight cassiterite, and on the bottom row the scale is clipped at 15000 so that lighter minerals are distinguishable. Note that only 8 of the 26 neighbours of a voxel are shown in 2D, thus the neighbour phase used to classify a voxel (denser neighbour voxel) may not be visible in the cross-section. Red arrows point to neighbour cassiterite grains where the interphase can be distinguished only at high resolution. White arrows point to small grains that are segmented at high resolution but not at low resolution.

4.2.2. Voxel intensity to cassiterite volume

Total volume of cassiterite (V_{total}) is calculated using the volume of all voxels containing only cassiterite (V_{bulk}), and the sum of the partial volumes of all interphase cassiterite voxels (intensities <46000). The volume fractions in a voxel are calculated using the linear regression corresponding to the voxel's neighbour based labelling in **Figure 4** (Eq. 2).

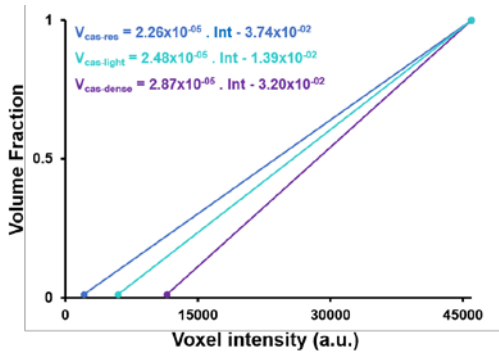


Figure 4: Volume fraction of cassiterite per voxel as a function of the voxel intensity. Three linear regressions and their equations are presented, one for each neighbour phase (resin – dark blue, lighter minerals – light blue and denser minerals – purple).

$$V_{total} = V_{bulk} + \sum V_{cas-res} + \sum V_{cas-light} + \sum V_{cas-dense} \quad \text{Eq. 2}$$

The value 0 % of cassiterite at the lowest intensity that defines a neighbour phase seems reasonable when compared to the detectable volume fraction of iodine and gold < 0.1 % found by Galper et al., 2012 and Bernstein et al., 2016. Even if the minimum detectable volume fraction of cassiterite would be 1%, the small shift in the linear regressions would be negligible in the total volume calculation. Nevertheless, it is anticipated that if the mineral of interest would have lower attenuation contrast or a value closer to the second distinguishable mineral (i.e. shorter intensity range of interphase voxels) the detectability would decrease. It is important to highlight that even if the classification of neighbours is incorrect for some voxels, the impact in the total volume is limited by the amplitude of possible volume fractions, i.e. the difference between the blue and purple lines for a given voxel intensity.

4.2.3. Validation of the new method

Here, we discuss the validity of the proposed method to calculate the volume of cassiterite by comparing the results from bulk chemical analysis, 2D SEM imaging and CT. Since no technique is perfect, results from a technique may not be reproduced by another. Therefore, a method is validated if a convergence between results from different techniques is achieved and this convergence is more pronounced than when using, for example, other segmentation methods. With that purpose, the higher 2D resolution of BSE and MLA and the more precise bulk elemental composition determined by XRF and ICP (coloured bands in **Figure 5a**) are compared to the volume fractions of cassiterite derived using the new method (crosses in **Figure 5a**, bold values in **Table 1**). A good agreement, within 10 % deviation (uncertainty of XRF measurement), between MLA/XRF and CT results is found for *ParVox* higher than 4.8, i.e. all resolutions of samples GM630 and GM250. Deviations above 10 % and up to 47 % (*ParVox* = 1.7) are measured for sample GM100. The larger deviations are associated to an underestimation of cassiterite, possibly caused by the under-segmentation of small grains and failure of the segmentation workflow to correctly label neighbour phases, visible in **Figure 3**. The seemingly over-segmented interphases do not translate into an overestimation of cassiterite volumes since interphase voxels only contribute to the total volume with a fraction of their volume.

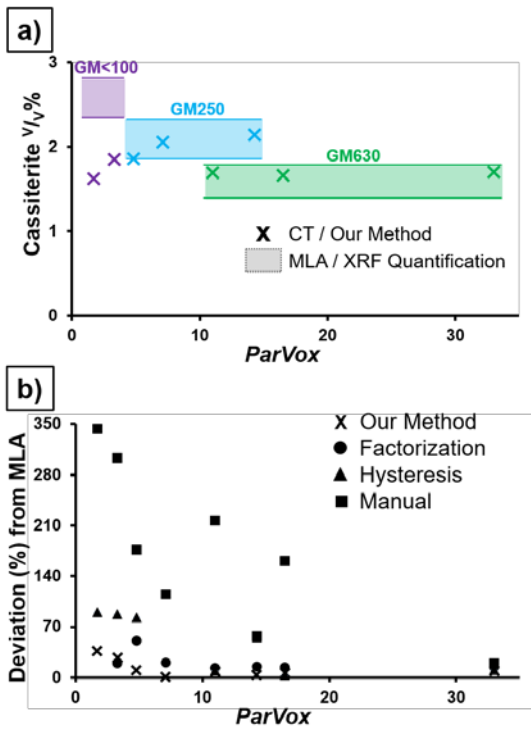


Figure 5: Particle to voxel size ratio (*ParVox*) as a function of **a)** volume percent of cassiterite derived using our method (crosses) and using MLA and XRF (color bands that mark the 10 % deviation from XRF). **b)** comparison of the deviation percentage between the volume of cassiterite derived from MLA and from CT using different segmentation methods.

Table 1: Volume percent of cassiterite (V_V %) measured using MLA and bulk chemical analysis, or using CT for each *ParVox* studied. CT values were derived using our method, manual threshold, or automatic segmentation methods (factorization or hysteresis).

	<i>GM630</i> (V_V) %			<i>GM250</i> (V_V) %			<i>GM<100</i> (V_V) %	
MLA	1.62			2.12			2.61	
Our method	1.70	1.66	1.69	2.14	2.05	1.86	1.85	1.62
Hysteresis	1.40	1.61	1.41	0.92	10.34	0.36	0.32	0.24
Factorization	1.78	1.78	1.77	2.37	2.48	3.11	3.05	37.36
Manual	1.94	4.22	5.14	3.33	4.55	5.87	9.03	9.89
ParVox ratio	33.0	16.5	11.0	14.3	7.1	4.8	3.3	1.7

Results from manual threshold and automatic segmentation methods, hysteresis and factorization, are compared to the results from our method (**Figures 5b and 6, Table 1**). The hysteresis method under-segments voxels at the edge of cassiterite particles and fails to identify smaller grains (e.g. red arrow, **Figure 6**). The under-segmentation is enhanced at lower resolutions and smaller particle sizes. This is a problem common for methods that use the computation of grey-scale gradients as the first step to segment particles with sizes close to the voxel size, mostly because a minimum intensity is necessary for a particle to be recognized, e.g. hysteresis and watershed segmentation (Drever et al. 2007). The factorization method results in more voxels labelled at cassiterite interphases and the segmentation of smaller cassiterite grains when compared to the hysteresis method. Thereafter, the volume of cassiterite is under-estimated by the hysteresis method and over-estimated by the factorization method. The factorization method yields fair deviations from MLA/XRF (<20 % for *ParVox* > 5) and the deviation is similar for each resolution but abruptly varies for each particle size. This suggests that the factorization method is more dependent on particle sizes and less dependent on the scan resolution, which means the method would be less adequate to compare natural samples that can contain a variety of grain sizes. Interestingly, the factorization method over-estimates the total volume of cassiterite even though it fails to identify small grains of cassiterite (yellow arrow, **Figure 6**), which means larger grains must be over-segmented. The manual threshold method results in a significant over-estimation of

cassiterite volumes and the deviation does not follow an obvious trend with the *ParVox*, which is possibly due to the bias of choosing a threshold value. From the four methods tested, the novel one performs better identifying small cassiterite grains, yields smaller deviations from MLA/XRF and the deviation of cassiterite percent shows a more consistent evolution as a function of *ParVox*. This validates our method as less bias, more accurate and less dependent on the particle size and on the resolution of the scan.

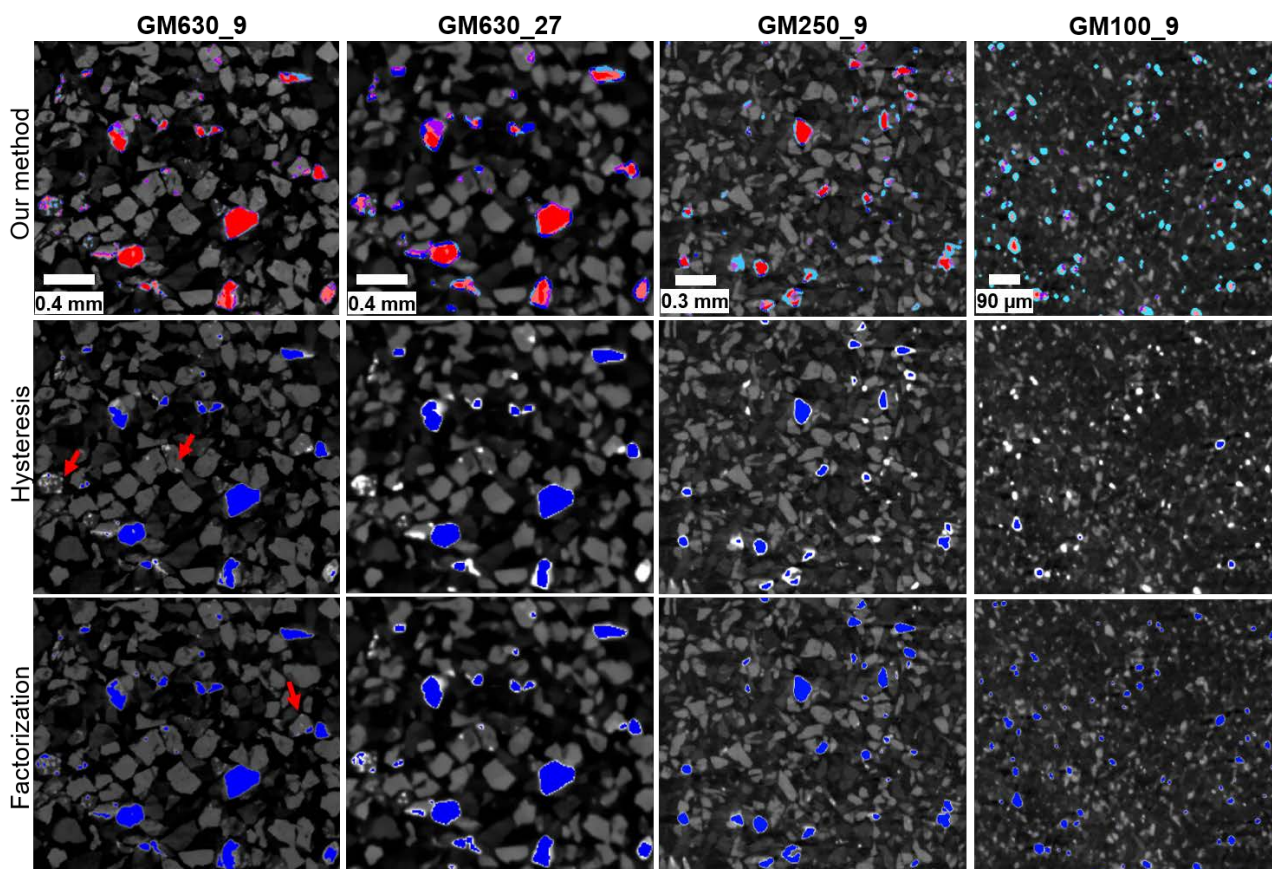


Figure 6: Cross-sections of CT datasets segmented using hysteresis and factorization methods and using our method. Red arrows point to cassiterite grains not labelled by the hysteresis method. Yellow arrow points to cassiterite particles not labelled by the factorization method.

4.3. Application of the new method

The new method is applied to quantify the volume of cassiterite in an uncrushed sample. With this purpose, a block of skarn ore was scanned under the same conditions as the grain mounts (**Figure 7**). The resulting histogram is similar to the histogram of grain mounts, whereby the peaks of cassiterite, denser and lighter minerals appear at intensity ranges similar to scan GM630_9, which suggests a similar mineral composition. As expected, the peak below 2100 is not present in the block, since it corresponds to the resin in the grain mounts.

The block is characterized by two major zones, one amphibole-rich (low density minerals, light blue) and another iron oxide-rich (high density minerals, dark blue). Both zones are crosscut by genetically late veins of precipitated quartz-chlorite-fluorite-sulphide assemblage that contain cassiterite with distinguishable sizes (**Figure 7 and Video 1**). The amphibole-rich zone contains 0.23% cassiterite as large grains and the iron oxide-rich zone contains 1.89% cassiterite as smaller grains that cover vein selvages, seemingly forming a continuous cassiterite phase. The different colours that represent cassiterite (red-yellow) are an indication of voxel intensities as shown by the colour-scale in the histogram in **Figure 7b**, i.e. orange to yellow tones represent bulk cassiterite (higher intensities) and red tones represent interphase cassiterite (lower intensity). The histogram indicates that the majority of cassiterite is represented by interphase voxels, thus small grain sizes

are expected. Therefore, using the new method, in contrast to other methods that fail to segment small grains, is expected to yield more accurate volume measurements and reduced bias. Furthermore, CT values are more representative than surface techniques that cannot accurately measure the amount of cassiterite in heterogeneous uncrushed samples. CT is also the only technique that would allow performing location-specific quantification, e.g. amount of cassiterite in each lithologic unit.

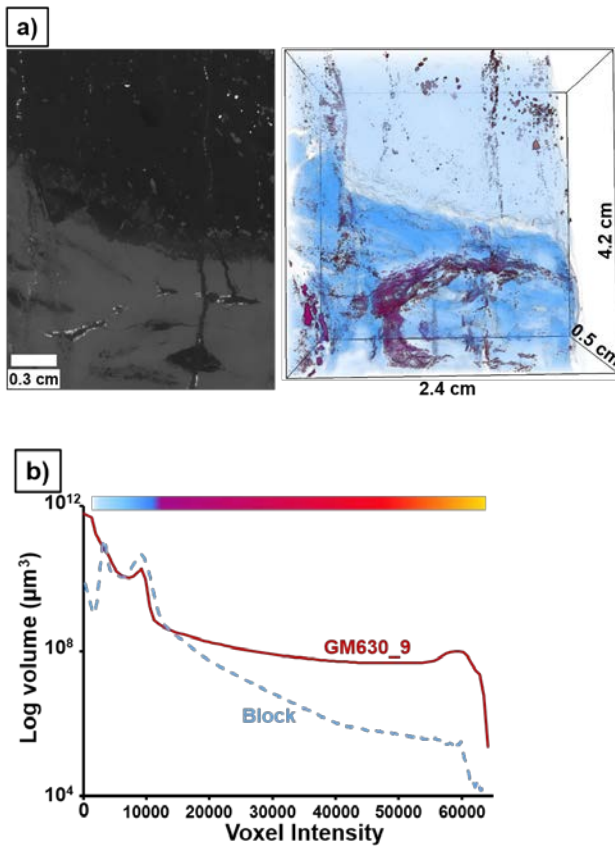


Figure 7: CT data of the block of skarn ore. **a)** Cross-section and 3D representation. In the cross-section, denser phases are shown brighter; and in 3D images cassiterite is represented in red-yellow, light minerals in light blue, dense minerals in darker blue and quartz (the least dense phase of light minerals) is set transparent to help highlight the cassiterite inside the veins. The colour scale is shown in **7b** associated to the histogram. **b)** The histograms of the block and sample GM630_9 are compared.

5. Discussion

The possibility of measuring the volume of smaller grains with improved accuracy using 3D imaging is expected to be useful to the broader field of ore geology and minerals engineering. The new method should be directly applicable to rocks and particulates with similar mineralogy, and also potentially applicable, with some optimization, to other mineral systems. For example, if the phase of interest is less dense than cassiterite, the X-ray energy used for scanning can be reduced in order to increase contrast between mineral groups. Another example, if mineral grains with a specific shape are dominant, a different workflow can be developed to help identifying the neighbour phases based also on shape. Consequently, it is advisable that image processing, scanning conditions and reconstruction parameters are refined for each mineral system and type of sample, using a similar correlative approach with other analytical techniques that can validate the method. Once the method is optimized, it should be applicable to any similar sample, e.g. similar ore-type. Since no special sample preparation is necessary (in contrast to MLA and chemical assays), such a method could be used for routine automated quantification of the ore mineralogy at different stages of beneficiation (Puvvada et al. 2019).

Generally, the lower ParVox for which this method gives an acceptable accuracy should be inversely proportional to the difference between attenuation contrasts of the mineral of interest and neighbour minerals. In the studied mineral system, cassiterite is represented by over 80 % of the total intensity range (**Figure 2b**), thus the quantification using our method is accurate even at low ParVox and single grains can be segmented as long as at least one voxel has intensity above 11500. Gold, silver, PGM and uranium deposits are examples of mineral systems where the phase of interest has high attenuation contrast against the gangue minerals, hence accurate volume quantification and improved particle segmentation at low ParVox are expected from our method. Another expected application is to quantify the volumetric content of small electronic components containing very dense phases (e.g. gold or tin), which is necessary to estimate the value and recoverability of recycling printed circuit boards. Our method is also expected to be applicable beyond the raw materials community. For example, in studies where the phase of interest is smaller than the voxel size but due to high attenuation contrast it can be qualitatively used to highlight a 3D region (Soulaine et al., 2016). This is, for example, the case in the medical industry where contrast agents are used to detect specific tissues (Qajar et al., 2013), or in the oil industry where fluids containing iodine are used to enhance connected nanoporous regions (Lin et al., 2016). Using our method, these qualitative strategies could potentially be made quantitative.

6. Conclusion

The method presented in this paper extends the applicability of CT to measure the volume of dense minerals in ore samples or in grain mounts by reducing the uncertainty of volume quantification, as well as lowering the limit of grain sizes for which volumes can be reliably measured using CT. Using a cassiterite ore as a case study, the method is shown to allow the quantification of volumes within 10 % deviation from the volumes measured by bulk chemical analysis and MLA when at least half of the particles are at least 5 times the voxel size of the CT scan. The method is validated using a feedback loop between complementary characterization techniques where the advantages of each technique are used to correct for the limitations of another. For example, minerals represented in the relative CT intensity scale are classified using BSE/MLA images. The reduced bias and uncertainty of measuring the volume of small and dense minerals, typical of ores, will broaden the application of 3D imaging in ore characterization.

6. Acknowledgements

We thank members of the BMBF-funded AFK Project (grant number 033R128) for supplying the bulk samples, particularly I. Bremerstein (UVR-FIA GmbH) for crushing, blending, splitting, and size classification. We would like to thank K. Graebe (HIF) for determining the particle sizes of samples. T. Jeske (Technical University Bergakademie Freiberg) is acknowledged for collecting the hand specimen that was analyzed.

7. References

- Bernstein, A.L., Dhanantwari, A., Jurcova, M., Cheheltani, R., Naha, P. C., Ivanc, T., Shefer, E., Cormode, D. P., 2016. Improved sensitivity of computed tomography towards iodine and gold nanoparticle contrast agents via iterative reconstruction methods. *Sci. Rep.*, 6, 26177 <http://dx.doi.org/10.1038/srep26177>
- Boas, F.E., Fleischmann, D., 2012. CT artifacts: Causes and reduction techniques. *Imag. Med.* 4(2), 229-240.
- Burnett, T.L., McDonald, S.A., Gholinia, A., Geurts, R., Janus, M., Slater, T., Haigh, S.J., Ornek, C., Almuaili, F., Engelberg, D.L., Thompson, G.E., Withers, P.J., 2014. Correlative Tomography. *Sci. Rep.* 4, 4711.

Chryssoulis, S.L., Cabri, L.J. 1990. Significance of gold mineralogical balances in mineral processing. *T. I. Min. Metall. C* 99, 1–10.

Cordes, N.L., Seshadri, S., Havrilla, G.J., Yuan, X., Feser, M., Patterson, B.M., 2015. Three Dimensional Subsurface Elemental identification of Minerals using Confocal Micro X-ray Fluorescence and Micro X-ray Computed Tomography. *Spect. Acta B.* 103–104, 144-154. doi.org/10.1016/j.sab.2014.12.006

Drever, L., Roa, W., McEwan, A., Robinson, D. 2007. Comparison of three image segmentation techniques for target volume delineation in positron emission tomography. *J. Appl. Clin. Med. Phys.*, 8, 83-109.

Fandrich, R., Gu, Y., Burrows, D., Moeller, K., 2007. Modern SEM-based mineral liberation analysis. *Intern. J. Min. Proc.* 84(1-4), 310-320.

Frenzel, M., Bachmann, K., Carvalho, J.R.S., Relvas, J.M.R.S., Pacheco, N., Gutzmer, J. 2018. The geometallurgical assessment of by-products—geochemical proxies for the complex mineralogical department of indium at Neves-Corvo, Portugal. *Miner. Deposita.* doi:10.1007/s00126-018-0849-6

Furat, O., Leißner, T., Ditscherlein, R., Šedivý, O., Weber, M., Bachmann, K., Gutzmer, J., Peuker, U. Schmidt, V., 2018. Description of Ore Particles from X-Ray Microtomography (XMT) Images, Supported by Scanning Electron Microscope (SEM)-Based Image Analysis. *Microsc.Microanal.* 24, 461-470

Galper, M.W., Saung, M.T., Fuster, V., Roessl E., Thran A., Proksa, R., Fayad, Z.A., Cormode, D. P., 2012. Effect of Computed Tomography Scanning Parameters on Gold Nanoparticle and Iodine Contrast. *Invest. Rad.* 47, 8, 475-481.

Glasbey, C.A., 1993. An analysis of histogram-based thresholding algorithms. *Graph. Mod. Im. Process.*, 55, 532-537.

Glover, G.H, Pelc, N.J., 1980. Nonlinear partial volume artifacts in x-ray computed tomography. *Med Phys.* 7, 238-48. DOI: 10.1118/1.594678

Godinho, J.R.A., Withers, P.J., 2018. Time-lapse 3D imaging of calcite precipitation in a microporous column. *Geochim. Cosmochim. Acta*, 222, 156-170.

Goodenough, D.J., Weaver, K.E., Costaridou, H., Eerdmans, H., Huysmans, P., 1986. A new software correction approach to volume averaging artifacts in CT. *Comput. Radiol.* 10, 2/3, 87–98.

Gu, Y., 2003. Automated Scanning Electron Microscope Based Mineral Liberation Analysis An Introduction to JKMR/FEI Mineral Liberation Analyser. *J. Min. Mat. Charac. Eng.* 2(1), 33-41.

Haines, B.B., Bettano, K.A., Chenard, M., Sevilla, R.S., Ware, C., Angagaw, M.H., Winkelmann, C.T., Tong, C., Reilly, J.F., Sur, C., Zhang, W., 2009. A Quantitative Volumetric Micro-Computed Tomography Method to Analyze Lung Tumors in Genetically Engineered Mouse Models. *Neoplasia* 11(1), 39–47.

Heckel, F., Meine, H., Moltz, J.H., Kuhnigk, J., Heverhagen, J.T., Kießling, A., Buerke, B., Hahn, H.K., 2014. Segmentation-Based Partial Volume Correction for Volume Estimation of Solid Lesions in CT. *IEEE Trans. Med. Imag.* 33, 462 - 480. 10.1109/TMI.2013.2287374

Heinig, T., Bachmann, K., Tolosana-Delgado, R., Van den Boogart, K. G., Gutzmer, J., 2015. Monitoring gravitational and particle shape settling effects on MLA sample preparation. *Proceed.*

IAMG 2015, 17th Annual Conference of the International Association for Mathematical Geosciences, 200–206.

Hoal, K.O., Stammer, J.G., Appleby, S.K., Botha, J., Ross, J.K., Botha, P.W., 2009. Research in quantitative mineralogy: Examples from diverse applications. *Min. Eng.* 22(4), 402-408.

Jayasree M., Narayanan N. K., Kabeer V., Arun C. R., 2018. An enhanced block based edge detection technique using hysteresis thresholding. *Signal & Image Processing*, 9, 15-26.

Kern, M., Möckel, R., Krause, J., Teichmann, J., Gutzmer, J., 2018a. Calculating the deportment of a fine-grained and compositionally complex Sn skarn with a modified approach for automated mineralogy: *Min. Eng.*, 116, 213-225. doi:10.1016/j.mineng.2017.06.006

Kern, M., Kästner, J., Tolosana-Delgado, R., Jeske, T., Gutzmer, J., 2018b. The inherent link between genesis and geometallurgy as documented by complex Sn mineralization at the Hämmerlein deposit (Erzgebirge, Germany). *Min. Dep.* doi:10.1007/s00126-018-0832-2

Ketcham, R.A., Carlson, W.D., 2001. Acquisition, optimization and interpretation of X-ray computed tomographic imagery: applications to the geosciences. *Comp. Geosci.* 27, 381–400.

Kornilov, A.S, Safonov, I.V., 2018. An Overview of Watershed Algorithm Implementations in Open Source Libraries. *J. Imag.* 4, 123. doi:10.3390/jimaging4100123

Kueh, A., Warnett, J.M., Gibbons, G.J., Brettschneider, J., Nichols, T.E., Williams, M.A., Kendall, W.S., 2016. Modelling the penumbra in Computed Tomography. *J. X-Ray Sci. Technol.* 24, 583–597. DOI 10.3233/XST-160576.

Lin, Q., Neethling, S.J., Dobson, K.J., Courtois, L., Lee, P.D., 2015. Quantifying and minimising systematic and random errors in X-ray micro-tomography based volume measurements. *Comp. & Geosci.* 77, 1-7.

Lin, Q., Al-Khulaifi, Y., Blunt, M. J., Bijeljic, B., 2016. Quantification of sub-resolution porosity in carbonate rocks by applying high-salinity contrast brine using X-ray microtomography differential imaging. *Adv. Water Resour.* 96, 306-322. doi.org/10.1016/j.adwatres.2016.08.002

Maire, E., Withers, P.J., 2014. Quantitative X-ray tomography. *Int. Mater. Rev.* 59, 1-43.

Silva M., C., Sørensen, B., Aasly, K., Ellefmo, S., 2018. Geometallurgical Approach to the Element-to-Mineral Conversion for the Nabbaren Nepheline Syenite Deposit. *Miner.* 8(8), 325. doi:10.3390/min8080325

Miller, J.D., Lin, C.L., Hupka, L., Al-Wakeel, M. I., 2009. Liberation-limited grade/recovery curves from X-ray micro CT analysis of feed material for the evaluation of separation efficiency. *Int. J. Min. Process.* 93, 48-53.

Miller, J.D., Lin, C.L., 2018. X-ray tomography for mineral processing technology – 3D particle characterization from mine to mill. *Min. Metal. Process.* 35, 1-12.

Parian, M., Lamberg, P., Möckel, R., & Rosenkranz, J., 2015. Analysis of mineral grades for geometallurgy: Combined element-to-mineral conversion and quantitative X-ray diffraction. *Min. Eng.*, 82, 25-35. doi:10.1016/j.mineng.2015.04.023

Puvvada, S., Lin, C.L., Miller, J.D., 2019. High speed X-ray computed tomography for plant-site analysis of pebble phosphate. *Minerals Engineering* 130, 129-141.

- Qajar, J., Francois, N., Arns, C. H., 2013. Microtomographic Characterization of Dissolution-Induced Local Porosity Changes Including Fines Migration in Carbonate Rock. *Soc. Petrol. Eng.* 18, SPE-153216-PA. doi:10.2118/153216-PA
- Reyes, F., Lin, Q., Udoudo, O., Dodds, C., Lee, P.D., Neethling, S.J., 2017. Calibrated X-ray micro-tomography for mineral ore quantification. *Min. Eng.* 110, 122-130.
- Reyes, F., Lin, Q., Cilliers, J.J., Neethling, S.J., 2018. Quantifying mineral liberation by particle grade and surface exposure using X-ray microCT. *Min. Eng.* 125, 75-82.
- Sezgin, M., Sankur, B., 2004. Survey over image thresholding techniques and quantitative performance evaluation. *J. Electr. Imaging* 13, 146–165.
- Soulaine, C., Gjetvaj, F., Garing, C., Roman, S., Russian, A., Gouze, P., Tchelepi, H.A., 2016. The Impact of Sub-Resolution Porosity of X-ray Microtomography Images on the Permeability. *Transp. Porous Med.* 113, 227-243. doi.org/10.1007/s11242-016-0690-2
- Ueda, T., 2018. Experimental analysis of mineral liberation and stereological bias based on X-ray computed tomography and artificial binary particles. *Adv. Powder. Tech.* 29, 462-470.
- Wang, Y., Burnett, T.L., Chai, Y., Soutis, C., Hogg, P.J, Withers P.J., 2017a. X-ray computed tomography study of kink bands in unidirectional composites. *Comp. Struc.* 160, 917-924. doi.org/10.1016/j.compstruct.2016.10.124
- Wang, Y., Lin, C.L., Miller, J.D., 2017b. Quantitative analysis of exposed grain surface area for multiphase particles using X-ray microtomography. *Powder Technol.* 308, 368–377.
- Wang, Y., McClung, C., Lin, C.L., Miller, J.D., 2018. Stereological correction of perimeter based estimates of exposed grain surface area. *Min. Eng.* 126, 64–73.
- Wills, B.A., Finch, J.A., 2016. *Wills' Mineral Processing Technology. An Introduction to the Practical Aspects of Ore Treatment and Mineral Recovery* (8 ed.). Amsterdam: Elsevier.